Fabrication of silicon nitride membrane nanoelectromechanical resonator

Hao Xu, Srisaran Venkatachalam, Christophe Boyaval, Pascal Tilmant, Francois Vaurette, Yves Deblock, Didier Theron, Xin Zhou

Fabrication of silicon nitride membrane nanoelectromechanical resonator

Hao Xu, Srisaran Venkatachalam, Christophe Boyaval, Pascal Tilmant, Francois Vaurette, Yves Deblock, Didier Theron, and Xin Zhou

***Abstract*—In this work, we present details of the nanofabrication process for achieving a silicon nitride nanoelectromechanical resonator, consisting of a membrane covered with a thin aluminium layer capacitively coupled to a suspended top gate. Critical nanofabrication steps have been discussed, including the XeF_2 selective etching process to release the silicon nitride membrane from the substrate and the reflow process to fabricate a top gate of a suspended membrane. This ultra-clean and CMOS-compatible process allows the silicon nitride membrane to have a high quality factor ($\sim$1.1$\times 10^4$) at room temperature and offers access to electrical integration with external circuits with high efficiency. In addition, we also demonstrate parametric amplification and de-amplification of the input signals by exploiting this suspended top gate. The measurement results of phase-sensitive amplifications have also been well fit by analytical caculations. The present work provides essential building blocks for further exploration of silicon nitride membrane based nanoelectromechanical resonators that can be efficiently integrated into large-scale electrical circuits.**

***Index Terms*—Silicon nitride membrane, nanofabrication, nanoelectromechanical resonator, parametric amplification**

I. Introduction

MICRO- and nano- electromechanical systems (MEMS/NEMS) have been promising candidates to be compliantly integrated with electrical circuits for various applications, in particular sensing such as pressure sensor[1][2], accelerometer[3], gyroscope [4] or thermometry [5]. Having electrostatic transductions has been widely applied in high frequency electrical system, because it gives an access to low power operation, offers a simple method for electrical integration, and allows MEMS/NEMS to have the higher resonance frequency [6]. In recent years, capacitive transduction schemes become very successful and have been widely used in MEMS applications, such as microphones [7][8]and pressure sensors [9]. Besides, resonance frequency tunability can be easily achieved by exploiting electrostatic forces. In addition, capacitive coupling schemes bring flexibility in explorations of coupled nanoelectromechanical resonators [10]. They are attractive for building mechanical resonator based quantum sensors thanks to their roles as passive elements in the capacitive coupled circuits [11], [12], [13].

Previous works have used various materials for fabricating nanoelectromechanical resonators with capacitive transduction, such as aluminium membrane [12], silicon nanowires [14], silicon nitride [5], [15], and graphene [16], [17]. Membrane-based MEMS and NEMS are very interesting because they allow mechanical displacement to be coupled more efficiently to external electrical circuits, potentially with low-power advantages. Very recently, silicon nitride membrane resonator has been achieved in on-chip integration with microwave optomechanical circuits [15]. Compared with typical silicon nitride beam design, more than 10 times coupling strength has been attainable in a silicon nitride membrane resonator. In addition, its unique structure and good mechanical properties allow the study of coupled nanoelectromechanical resonators and stochastic switching at room temperature [10], [18]. Such a device is promising for achieving large-scale coupled NEMS, which can be used for phonon-based signal processors. It also shows potential for use in today's quantum signal processing. So far, the critical fabrication process (as shown in Fig.1) and the parametric amplification capability of such a promising device have not yet been analysed and

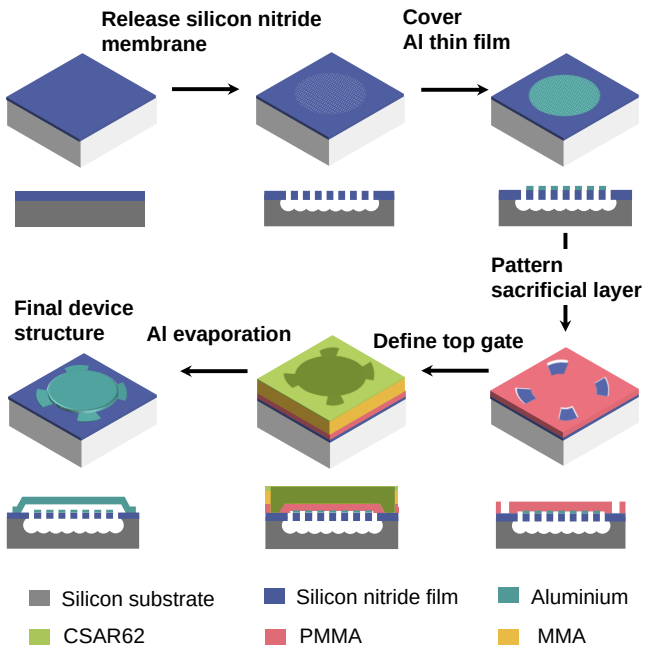

Fig. 1. Schematic of nanofabrication process for a silicon nitride drum nanoelectromechanical resonator. It includes the dry etching process to release the membrane from the substrate, the deposition of a metal layer on the surface of the membrane and the two-step lithography process to create a suspended top gate.

The authors are with CNRS, Université Lille, Centrale Lille,Université Polytechnique Hauts-de-France, UMR8520, IEMN, Av. Henri Poincare, Villeneuve d'Ascq 59650, France (Corresponding e-mail: xin.zhou@cnrs.fr).

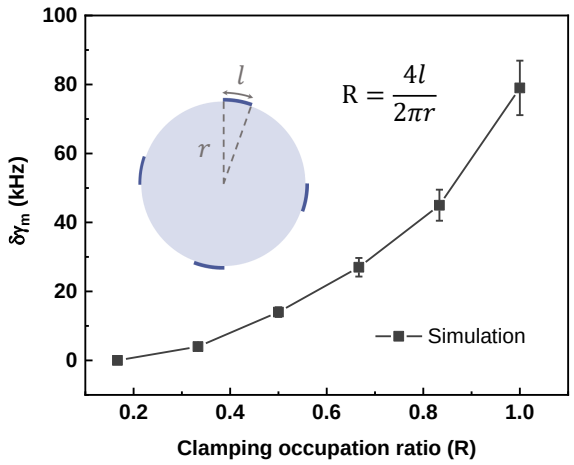

Fig. 2. Simulation results of mechanical damping rates of a circular membrane, corresponding to different clamping ratio $R = \frac{4l}{2\pi r}$. The insets are the schematic for the definition of clamping occupation ratio, where the dark blue shows the clamping part of the membrane. Here, r is the radius of the circular membrane.

discussed, although they are important for further optimizing device performance and for attracting more research interest from the MEMS/NEMS community.

In this work, we discuss fabrication details of a membrane nanoelectromechanical resonator made of a silicon nitride membrane covered by a thin aluminium film, which is capacitively coupled to external circuits by its suspended top gate. Using finite element method (FEM), we have investigated damping rates of the circular membrane, which helps us to optimise the design and to understand trade-off between achieving low clamping losses and feasible fabrication process. Two key nanofabrication steps have been discussed, including releasing of the silicon nitride membrane from the silicon substrate and forming a suspended gate, in order to provide essential guidance for the critical dry selective etching process and reflow processes. In addition, to demonstrate the functionality of the suspended gate, we also characterize non-degenerate parametric amplifications with different frequency detuning. The pump phase dependence gain, in a degenerate parametric pumping scheme, has also been measured.

II. Device Fabrication

First, in order to optimise the design, we also exploit the finite element method to simulate the clamping losses of the silicon nitride circular membrane with a fixed tensile stress and diameter, giving a resonance frequency ∼1.353 MHz. The clamping occupation ratio R is defined to be the total arc length ($4l$) of the clamping edge over the circumference ($2\pi r$). The simulation results are shown in Fig. 2. The simulation results of damping rate $\delta\gamma_m$ are obtained by normalizing the damping rate γ_m with the γ_m = 9.4 kHz simulated with the value $R = \frac{1}{6}$, namely $\delta\gamma_m = \gamma_m$-$\gamma_m(R = \frac{1}{6})$. Obviously, the value of $\delta\gamma_m$ increases as the R increases. Our device, actually, consists of two membranes, the aluminium membrane acting as a suspended top gate and the silicon nitride membrane drum. For the silicon nitride membrane nanomechanical resonators, the dissipation is highly diluted by its high tensile stress [19]. In recent years, soft clamping schemes have been exploited to further reduce damping effects, where most of the silicon nitride membrane edges are etched away to avoid full clamping [20]. Such membrane nanomechanical resonators are well suited for applications in optical systems. However, it is very challenging to achieve electrical integration of this type of the membrane, as the membrane becomes too fragile to fabricate a suspended top gate. Considering the difficulties in the fabrication process, we therefore design the silicon nitride membrane to be a fully clamped scheme in this work. In order to have a capacitive coupling scheme, a thin aluminium layer will be deposited on surface of the silicon nitride membrane. It is designed not to cover the entire clamping edge of the silicon nitride membrane, but only the edge where the two leads are connected (as shown in the Fig.4(a)), with the R $<$ 0.2, so as to reduce additional clamping losses. Besides, we would like to mention that the aluminium top gate is also a nanoelectromechancial resonator, with resonance frequency around $\sim$ 3 MHz [10]. In order to reduce its clamping losses, the clamping ratio R=0.5 is chosen. In the following part, we only focus on discussion of the silicon nitride membrane resonator.

The nanofabrication process of this device starts from an intrinsic silicon substrate with high resistivity ∼10 kΩ·cm, covered with a stoichiometric silicon nitride (Si_3N_4) thin film, 100 nm in thickness. The tensile stress of this silicon nitride layer is ∼1.0 GPa. Fig.1 shows nanofabrication process of a silicon nitride drum mechanical resonator. It includes two critical steps: (i) release of silicon nitride membrane from the silicon substrate and (ii) form an aluminium suspended gate on the top of the membrane.

(i) The method of releasing the silicon nitride membrane from the substrate consists of two steps dry etching process by using electron beam resist as an etching mask. We first define the nominal diameter of the vibrating membrane by using electron beam (EB) lithography and development process to pattern circular symmetric holes on the CSAR62 resist [21]. These holes are defined to be $\sim$ 300 nm in diameter and the distance between the nearest neighbour hole is ∼1.3 μm. The pattern is then transferred from the resist to the silicon nitride thin film by reactive ion etching (RIE) through these circular holes to remove unwanted parts. In this RIE process, sulfur hexafluoride (SF_6) and argon (Ar) with a flow rate of 10 sccm and active plasma power 30 Watt are exploited, giving rise to the etching rate of silicon nitride ∼20 nm/min. After removing the silicon nitride parts, the RIE process will continue to remove $\sim$ 350 nm silicon part from the substrate. It is critical for the subsequent xenon difluoride (XeF_2) etching process, as the XeF_2 has a highly selective etching rate between silicon and silicon nitride [22]. In our process, this rate is $\sim$ 100:1. To release the silicon nitride membrane, the chamber pressure is maintained at 2.2 Torr and we perform two cycles of etching, with 30 seconds etch time per cycle. This gives the maximal etching rate of Si, ∼70.4 nm/s. This rate highly depends on the exposure area for etching and the doping density of the silicon substrate. Fig.3 shows scanning electron microscope (SEM) images of silicon nitride membranes. Once the membrane is

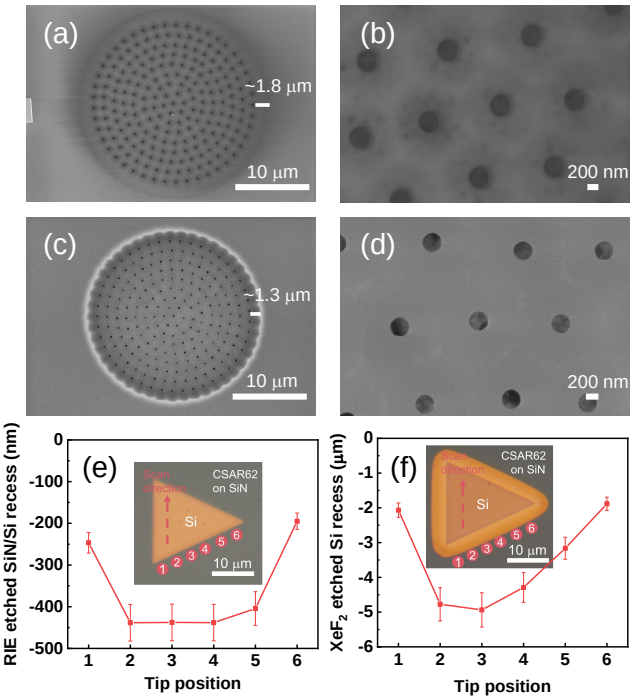

Fig. 3. SEM images, the top view of silicon nitride membrane. (a) Well-released silicon nitride membrane and (b) circular etch holes. (c) and (d) Partly released membrane and these etch holes. (e) Profilometry measurement results of RIE etching of a silicon nitride thin film (100 nm) on top of a silicon substrate through a triangular window. The inset is an optical image of this triangle pattern. The moving direction of the tip which has been implemented to measure the etching step follows the direction of the red dashed arrow. Each red square corresponds to a measurement result for a different starting position of the red solid circles shown in the inset. (f) Etch result of the sample which has been through the RIE etch first and then the XeF_2 etch process.

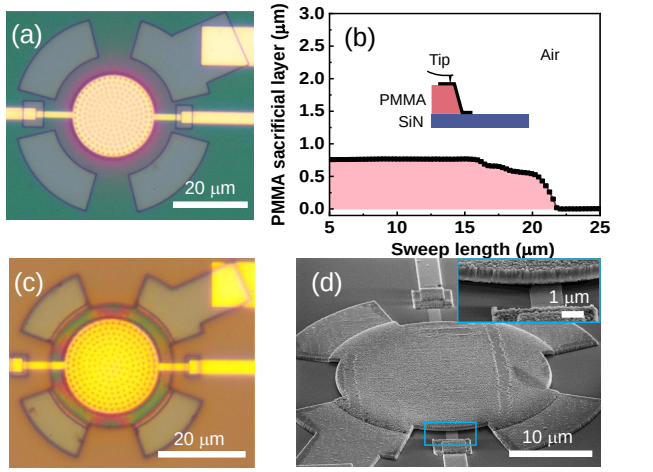

Fig. 4. Optical micrographs of top view of the support feet pattern. (a) Optical images showing the pattern development of the support feet before the reflow process. (b) Profilometry measurement of the PMMA resist after the reflow process. (c) Top gate patterned on the resists through EB lithography, followed by development. (d) Final device structure, where the inset shows the gap between the drum membrane and the Al top gate.

well released from the silicon substrate, the undercut between the clamping edge and the outer hole is around $\sim$1.8 μm, as shown in Fig.3(a). This indicates that lateral etching of the silicon portion between two nearest neighbour holes under the silicon nitride film is sufficient to release the membrane from the substrate. No particles and etch residues adhere to the underside of the membrane, as shown in Fig.3(b), which are crucial to access the good mechanical properties. Fig.3(c) and (d) indicate an insufficient etching example. The undercut is not large enough and the etch residue exists below the membrane that can be observed through these holes. The mechanical resonator cannot vibrate properly in this case.

In order to survey the etching process, a triangular pattern is designed by exposing CSAR62 resist, positioning near the drum structure. Fig.3(e) and (f) show the etch results of these triangular designs, for RIE and XeF_2 process, respectively. At the same etching condition in RIE process, $\sim$430 nm of materials (100 nm of silicon nitride and $\sim$330 nm of silicon) have been removed at the centre part of this pattern. While, for the position near the pattern edge, only $\sim$200 nm materials have been etched away. In the following step of XeF_2 etching, $\sim$2 μm silicon has been removed near the edge of the triangular pattern. The undercut is around $\sim 4\mu$m, as shown in Fig.3 (f). This is consistent with the fact that the XeF_2 etching rate highly depends on the exposure area for etching.

After dry etching process mentioned above, an aluminium thin film 30 nm in thickness is deposited on the surface of the suspended silicon nitride membrane through evaporation process. This thin metal layer allows the silicon nitride membrane to be capacitively coupled to an external gate electrode and to be driven by electrostatic forces. It is deserved to mention that some part of the aluminium layer goes through those patterned holes to the underneath silicon substrate, forming a stray capacitance. Considering the depth of the silicon layer removed in the etching process, $> 2\mu$m, this stray capacitance is quite small compared to the gate capacitance, so we could neglect its effect on the overall electrical performance of the device. The mechanical properties of the membrane are still dominated by the silicon nitride layer having the high tensile stress, and the resonant frequency of the membrane is not reduced too much by the extra mass added by this thin aluminium layer.

(ii) The second critical step is to fabricate a suspended top gate of the silicon nitride drum covered with an aluminium thin film, forming a capacitive coupling scheme. This process is inspired by the nanofabrication process of air-bridge in superconducting quantum circuits [23]. In our work, we use either PMMA (methyl methacrylate) or PMGI (polydimethylglutarimide) EB resist as a sacrificial layer. The thickness of this layer defines the distance between the silicon nitride membrane and its suspended gate. The resist will first be soft baked at the relatively low temperature $\sim$150 °C. After patterning the feet of the suspended gate through EB lithography and development process, the resist is then baked at the higher temperature $\sim$180 °C. It is well known as the reflow process, where the edges of the pattern are rounded and cannot give rise to a lift-off process. Fig.4 (a) shows an optical image of the patterned PMMA resist after development. After the reflow process, the pattern exhibits traces near the rounded edge, as shown in Fig.4(b). Then, the sample is coated with a bilayer of EB resist, 2 μm thick

MMA (methyl methacrylate), and ∼120 nm thin CSAR62 resist, which are suitable for the critical lift-off process. The final gate is patterned on this bilayer resist through lithography, followed by the development and deposition of the 550 nm thick Al film. The device fabrication process ends up after the lift-off process. Fig.4(d) shows the final device structure, where the top inset SEM image of the gap between the bottom electrode and its top gate.

III. Device Characterisation

After achieving the fabrication of the silicon nitride membrane nanoelectromechanical resonator, we combined an electrical ac signal V_{ac} and a dc signal V_{dc} to generate an electrostatic force for driving the device and used microwave reflectometry for readout [15], [10]. All measurements are performed at room temperature in a vacuum chamber ($\sim 10^{-6}$ mbar). The membrane, measured in this work, is 30 μm in diameter with resonance frequency $\Omega_m/2\pi \approx 11.83$ MHz and quality factor Q $\approx 1.1\times10^4$, at room temperature.

$$\begin{aligned} &m_{eff}\ddot{x} + m_{eff}\gamma_m\dot{x} + [\kappa + \delta\kappa \cdot Sin(\omega_p t + \varphi)]x \\ &= F_d \cdot Cos(\omega_s t) \end{aligned} \tag{1}$$

Capacitive coupling scheme allows to perform parametric operation by using an AC signal as a pump tone to modify the spring constant κ of the membrane, at the frequency ω_p. The motion equation Eq.1 is used to describe the basic principle of electromechanical parametric pumping [24]. Here, x is the mechanical displacement at the membrane location where it is maximal, γ_m is the mechanical damping, and m_{eff} is the effective mass of the vibrating structure. The driving force $F_d \cdot Cos(\omega_s t)$ is determined by a general expression: $\partial(C_g(x)(V_{dc} + V_{acs} \cdot Cos(\omega_s t))^2/2)/\partial x$. The ω_s is the frequency of drive force and φ is the phase of the pump signal. The $\delta\kappa \cdot Sin(\omega_p t + \varphi)$ is the modulation of the intrinsic spring constant κ, generated by the pump force, $\delta\kappa \cdot Sin(\omega_p t + \varphi) = (\partial F_p/\partial x) \cdot Sin(\omega_p t + \varphi) \approx 2C_{g0}V_{dc}V_{acp} \cdot Sin(\omega_p t + \varphi)/d^2$. The V_{acs} and V_{acp} are the amplitudes of AC signals for the drive and the pump tone respectively. According to different pumping schemes, in the following part, we will discuss measurement results in (i) non-degenerate pumping scheme: $\omega_p \neq 2\omega_s$, and (ii) degenerate pumping scheme: $\omega_p = 2\omega_s$.

(i) Non-degenerate pumping scheme, $\omega_p/2 = \omega_s - \delta$ and $\delta \neq 0$, as shown in Fig.5. The δ is the frequency difference between the half frequency of the pump tone $\omega_p/2$ and the frequency of the driving signal ω_s. Therefore, in this case, the phase difference φ between the pump and the drive signal can be ignored in the Eq.1, as it is arbitrary. Because of frequency mixing, in non-degenerate case, idler signal with frequency ω_i = $\omega_p - \omega_s$ is generated. By solving the motion equation Eq.1, the signal amplitude gain G_{sig} is obtained from the ratio of the signal amplitudes corresponding to the pump on and off states,

$$G_{sig} = \frac{1}{1 - \frac{\delta\kappa^2}{16\,(m_{eff}\Omega_m)^2\,\chi_s^{-1}\chi_i^{*-1}}}. \tag{2}$$

Here, $\chi_s = 1/(-\delta - i\gamma_m/2)$ and $\chi_i = 1/(\delta - i\gamma_m/2)$ are the susceptibilities of the mechanical resonator respectively

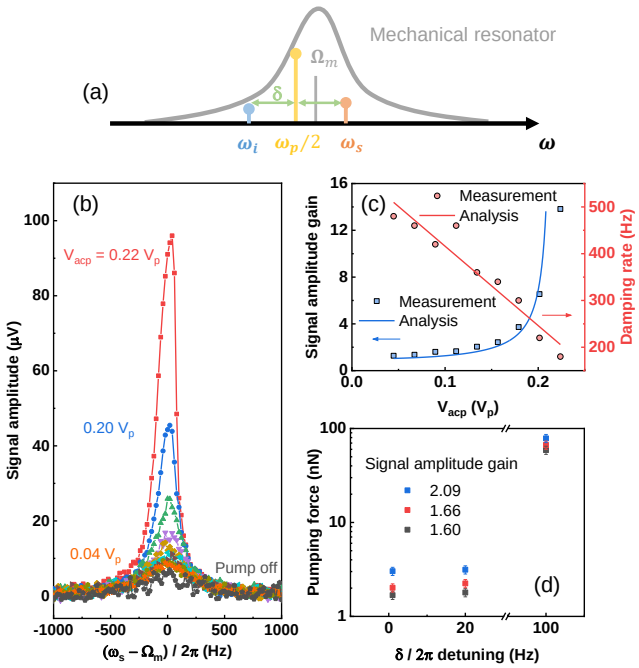

Fig. 5. (a) Non-degenerate parametric pumping scheme. (b) Parametric amplification of the input signal with frequency ω_s. The system is parametricly pumped at the frequency ω_p, with frequency detuning δ from the probe signal ω_s, δ=ω_s-$\omega_p/2$. (c) Signal amplitude gain as a function of pump amplitude V_{acp}, which is measured with $\delta/2\pi$=20 Hz. (d) Pumping forces correspond to different $\delta/2\pi$ = 1,20,100 Hz in order to reach the signal amplitude gain 2.09, 1.66, and 1.60 respectively.

corresponding to signal and idler. Its conjugate is indicated by the symbol "*". In the measurement of non-degenerate amplification, the device is driven at the frequency ω_s and is parametrically pumped at the frequency $2\omega_s + \delta$. Fig.5(b) shows the non-degenerate parametric amplification results corresponding to different pumping amplitudes, measured with $\delta/2\pi$ = 20 Hz, V_{dc} = 2 V, V_{acs} = 112 μV_p. For the higher pump amplitude, the mechanical responses exhibit slightly nonlinear behaviours. The signal amplitude gain at the frequency ω_s = Ω_m is shown in Fig.5(c), which is well fit by using Eq.2. As the pump amplitude (V_{acp}) increases, more energy is transduced to the mechanical system, resulting in the higher gain and the lower damping rates. Besides, we have also measured the signal gain as a function of detuning frequency δ. Fig.5(d) shows that the pump forces, required to achieve the same signal gain, are different relying on the δ. Obviously, the pump becomes more efficient as the δ decreases.

(ii) Degenerate pumping scheme, ω_p = $2\omega_s$. In the degenerate pumping scheme, the pump phase φ plays an important role in determining amplification and de-amplification. The degenerate gain is given by solving Eq.1,

$$G_{sig-deg} = \left|\frac{1 - \frac{Q\delta\kappa}{2\kappa} \cdot Cos(\varphi) - i\frac{Q\delta\kappa}{2\kappa} \cdot Sin(\varphi)}{(\frac{Q\delta\kappa}{2\kappa})^2 - 1}\right|. \tag{3}$$

In order to reach the maximum gain in the measurement, we choose to drive the resonator at its resonance frequency ω_m and pump it at the frequency $2\omega_m$. Fig.6(b) shows that the amplitude gain is sensitive to the phase that manipulates the

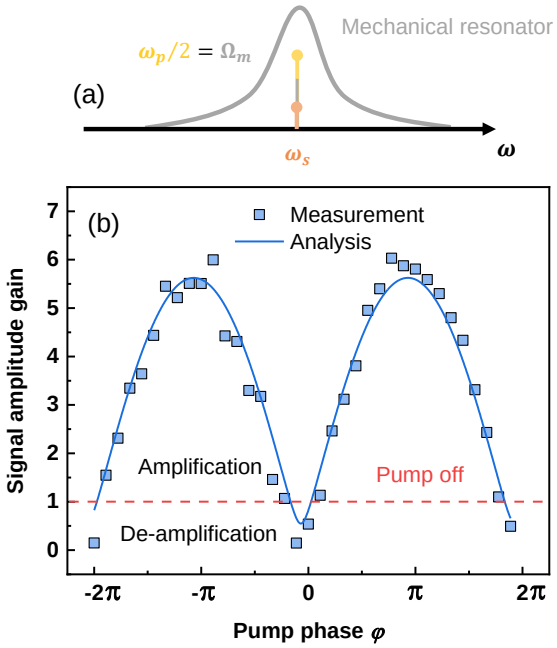

Fig. 6. Degenerate parametric pumping scheme. (a) Schematic of degenerate pumping used in the measured, $\omega_p = 2\omega_s = 2\Omega_m$. The vertical bars represent the position of the angular frequencies related to the schematic amplitude. (b) Solid squares, the signal amplitude gain as a function of pump phase φ, which are measured at V_{dc} = 2 V, V_{acs} = 201 μV_p for the amplitude of the driving signal ω_s, and V_{acp} = 0.19 V_p for the amplitude of the pump signal. The blue line is fitted by the Eq.3

signal to be amplified and de-amplified. The measurement data can be fitted well by the above analysis Eq.3 by using the parameters of quality factor Q $\approx$ 1.1 $\times 10^4$, the pump force used for the fit $F_{p,fit} \approx$ 4.74 nN corresponding to $\delta\kappa \approx 1.2\times10^{-2}$ N/m. It is obvious that this pump force agrees well with the experiment pumping force (V_{dc} = 2 V,V_{acp} = 0.19 V_p, $C_{g0} \approx 7.918 \times 10^{-15}$ F) $\approx$ 3.81 nN. Besides, the horizontal red line corresponds to the pump off (V_{acp}=0 V) and determines the threshold between amplification and de-amplification, showing the tunability of the mechanical gains. This degenerate parametric pumping scheme can be potentially used for sensing applications either in signal enhancement or for noise squeezing applications [25], [26].

IV. Conclusion

In summary, we have presented a detailed fabrication process to achieve a novel NEMS structure in which two suspended membranes are capacitively coupled. It consists of a silicon nitride membrane covered with an aluminium thin film capacitively coupled to a suspended aluminium top gate. Two key nanofabrication steps, including the dry etching process to release silicon nitride circular membrane and the reflow process to fabricate suspended top-gate, have been discussed. Compared to silicon nitride film nanoelectromechanical resonators fabricated by flip-chip technology [27], our fabrication process is relatively complex, but opens up opportunities for large-scale on-chip electrical integration. This ultra-clean fabrication process allows this device to have a high quality factor $\sim 1.1\times10^4$ with a resonance frequency $\Omega_m/2\pi \approx$ 11.83 MHz, at room temperature. Our membrane resonator offers a well-balanced compromise among the resonant frequency, the quality factor and the high coupling strength in comparison to the doubly-clamped beam nanoelectromechanical resonators that have been widely studied [28], [29], [30]. Besides, through finite element simulation, we also investigated the damping rate of the circular membrane that is dominated by the clamping losses. In addition, both parametric amplifications and de-amplifications of the input signal have also been demonstrated in this unique device structure. The present work paves the way for further exploration of silicon nitride based nanoelectromechanical resonators for electronically integrated large-scale circuits and quantum engineering.

Acknowledgment

Author contribution statements: H.X. performed the etching test, alpha-step measurement, and simulations, with helps from P.T., F.V., Y.D., C.B, and D.T.. All SEM images were taken by C.B and X.Z.. S.V. fabricated the NEMS devices and performed electrical (RF) measurement together with X.Z.. The results were analysed by H.X., D.T., and X.Z.. H.X. prepared the draft and X.Z. wrote the final version of the manuscript. All authors participated in discussions and revisions of the manuscript.

The authors would like to acknowledge financial support from STaRS-MOC Project No. 181386 the Region Hauts-de-France, from ISITE-MOST Project No. 201050, the French National Research Agency, ANR-MORETOME, No. ANR-22-CE24-0020-01, and Chist-ERA NOEMIA project with contract ANR-22-CHR4-0006-01.This work was partly supported by the French Renatech network.

References

[1] S. R. A. Ruth, V. R. Feig, H. Tran, and Z. Bao, "Microengineering pressure sensor active layers for improved performance," *Advanced Functional Materials*, vol. 30, no. 39, p. 2003491, 2020.

[2] P. Zhang, X. Cheng, Z. Zhou, Q. Zhang, W. Gu, D. Sun, and X. Huang, "An artificial neural network method for high-accurate and high-efficient mems pressure sensor design," *IEEE Sensors Journal*, vol. 22, no. 21, pp. 20 585–20 592, 2022.

[3] R. Kononchuk, J. Cai, F. Ellis, R. Thevamaran, and T. Kottos, "Exceptional-point-based accelerometers with enhanced signal-to-noise ratio," *Nature*, vol. 607, no. 7920, pp. 697–702, 2022.

[4] K. Liu, W. Zhang, W. Chen, K. Li, F. Dai, F. Cui, X. Wu, G. Ma, and Q. Xiao, "The development of micro-gyroscope technology," *Journal of Micromechanics and Microengineering*, vol. 19, no. 11, p. 113001, 2009.

[5] X. Zhou, D. Cattiaux, R. Gazizulin, A. Luck, O. Maillet, T. Crozes, J.-F. Motte, O. Bourgeois, A. Fefferman, and E. Collin, "On-chip thermometry for microwave optomechanics implemented in a nuclear demagnetization cryostat," *Physical Review Applied*, vol. 12, no. 4, p. 044066, 2019.

[6] S. Schmid, L. G. Villanueva, and M. L. Roukes, *Fundamentals of nanomechanical resonators*. Springer, 2016, vol. 49.

[7] G. Nicollini and D. Devecchi, "Mems capacitive microphones: acoustical, electrical, and hidden thermal-related issues," *IEEE Sensors Journal*, vol. 18, no. 13, pp. 5386–5394, 2018.

[8] B.-H. Kim and H.-S. Lee, "Acoustical-thermal noise in a capacitive mems microphone," *IEEE Sensors Journal*, vol. 15, no. 12, pp. 6853–6860, 2015.

[9] K. B. Balavalad and B. Sheeparamatti, "A critical review of mems capacitive pressure sensors," *Sensors & Transducers*, vol. 187, no. 4, p. 120, 2015.

[10] A. Pokharel, H. Xu, S. Venkatachalam, E. Collin, and X. Zhou, "Coupling capacitively distinct mechanical resonators for room-temperature phonon-cavity electromechanics," *Nano Letters*, vol. 22, no. 18, pp. 7351–7357, 2022.

[11] D. Cattiaux, I. Golokolenov, S. Kumar, M. Sillanpää, L. Mercier de Lépinay, R. Gazizulin, X. Zhou, A. Armour, O. Bourgeois, A. Fefferman, *et al.*, "A macroscopic object passively cooled into its quantum ground state of motion beyond single-mode cooling," *Nature communications*, vol. 12, no. 1, p. 6182, 2021.

[12] J. D. Teufel, T. Donner, D. Li, J. W. Harlow, M. Allman, K. Cicak, A. J. Sirois, J. D. Whittaker, K. W. Lehnert, and R. W. Simmonds, "Sideband cooling of micromechanical motion to the quantum ground state," *Nature*, vol. 475, no. 7356, pp. 359–363, 2011.

[13] N. R. Bernier, L. D. Toth, A. Koottandavida, M. A. Ioannou, D. Malz, A. Nunnenkamp, A. Feofanov, and T. Kippenberg, "Nonreciprocal reconfigurable microwave optomechanical circuit," *Nature communications*, vol. 8, no. 1, p. 604, 2017.

[14] Q. Yu, S. Li, A. M. Minor, J. Sun, and E. Ma, "High-strength titanium alloy nanopillars with stacking faults and enhanced plastic flow," *Applied Physics Letters*, vol. 100, no. 6, p. 063109, 2012.

[15] X. Zhou, S. Venkatachalam, R. Zhou, H. Xu, A. Pokharel, A. Fefferman, M. Zaknoune, and E. Collin, "High-q silicon nitride drum resonators strongly coupled to gates," *Nano Letters*, vol. 21, no. 13, pp. 5738–5744, 2021.

[16] X. Song, M. Oksanen, J. Li, P. Hakonen, and M. A. Sillanpää, "Graphene optomechanics realized at microwave frequencies," *Physical review letters*, vol. 113, no. 2, p. 027404, 2014.

[17] R. De Alba, F. Massel, I. R. Storch, T. Abhilash, A. Hui, P. L. McEuen, H. G. Craighead, and J. M. Parpia, "Tunable phonon-cavity coupling in graphene membranes," *Nature nanotechnology*, vol. 11, no. 9, pp. 741–746, 2016.

[18] S. Venkatachalam and X. Zhou, "Effects of stochastic forces on the nonlinear behaviour of a silicon nitride membrane nanoelectromechanical resonator," *Nanotechnology*, vol. 34, no. 21, p. 215202, 2023.

[19] S. S. Verbridge, J. M. Parpia, R. B. Reichenbach, L. M. Bellan, and H. G. Craighead, "High quality factor resonance at room temperature with nanostrings under high tensile stress," *Journal of Applied Physics*, vol. 99, no. 12, p. 124304, 2006.

[20] A. Barg, "Optomechanics with soft-clamped silicon nitride mambranes and carrier-mediated forces in coupled quantum wells," Ph.D. dissertation, University of Copenhagen, Faculty of Science,Niels Bohr Institute, Niels Bohr Institute, Danish Center for Quantum Optics, 2018.

[21] S. Thoms and D. S. Macintyre, "Investigation of csar 62, a new resist for electron beam lithography," *Journal of Vacuum Science & Technology B, Nanotechnology and Microelectronics: Materials, Processing, Measurement, and Phenomena*, vol. 32, no. 6, p. 06FJ01, 2014.

[22] F. I. Chang, R. Yeh, G. Lin, P. B. Chu, E. G. Hoffman, E. J. Kruglick, K. S. Pister, and M. H. Hecht, "Gas-phase silicon micromachining with xenon difluoride," in *Microelectronic structures and microelectromechanical devices for optical processing and multimedia applications*, vol. 2641. SPIE, 1995, pp. 117–128.

[23] M. Abuwasib, P. Krantz, and P. Delsing, "Fabrication of large dimension aluminum air-bridges for superconducting quantum circuits," *Journal of Vacuum Science & Technology B, Nanotechnology and Microelectronics: Materials, Processing, Measurement, and Phenomena*, vol. 31, no. 3, p. 031601, 2013.

[24] B. Hauer, C. Doolin, K. Beach, and J. Davis, "A general procedure for thermomechanical calibration of nano/micro-mechanical resonators," *Annals of Physics*, vol. 339, pp. 181–207, 2013.

[25] D. Rugar and P. Grütter, "Mechanical parametric amplification and thermomechanical noise squeezing," *Physical Review Letters*, vol. 67, no. 6, p. 699, 1991.

[26] X. Zhou, V. Schmitt, P. Bertet, D. Vion, W. Wustmann, V. Shumeiko, and D. Esteve, "High-gain weakly nonlinear flux-modulated josephson parametric amplifier using a squid array," *Physical Review B*, vol. 89, no. 21, p. 214517, 2014.

[27] M. Yuan, V. Singh, Y. M. Blanter, and G. A. Steele, "Large cooperativity and microkelvin cooling with a three-dimensional optomechanical cavity," *Nature communications*, vol. 6, no. 1, p. 8491, 2015.

[28] T. Faust, P. Krenn, S. Manus, J. P. Kotthaus, and E. M. Weig, "Microwave cavity-enhanced transduction for plug and play nanomechanics at room temperature," *Nature communications*, vol. 3, no. 1, p. 728, 2012.

[29] F. Massel, T. T. Heikkilä, J.-M. Pirkkalainen, S.-U. Cho, H. Saloniemi, P. J. Hakonen, and M. A. Sillanpää, "Microwave amplification with nanomechanical resonators," *Nature*, vol. 480, no. 7377, pp. 351–354, 2011.

[30] Y. Tsuchiya, Y. Feng, C. Giotis, N. Harada, M. Shikida, C. Dupré, E. Ollier, F. A. Hassani, and H. Mizuta, "Characteristic resonance features of soi-cmos-compatible silicon nanoelectromechanical doubly-clamped beams up to 330 mhz," in *2018 IEEE Micro Electro Mechanical Systems (MEMS)*. IEEE, 2018, pp. 515–518.